

The structural and optical response of the Au nanoparticles embedded in YSZ modified using high-energetic ion irradiation

Romana Mikšová^{1*}, Jakub Cajzl³, and Anna Macková^{1,2}

¹Nuclear Physics Institute of the Czech Academy of Sciences, p.r.i, 250 68 Řež, Czech Republic

²Department of Physics, Faculty of Science, J.E. Purkyně University, Pasteurova 3544/1, 400 96 Ústí nad Labem, Czech Republic

³Department of Inorganic Chemistry, University of Chemistry and Technology in Prague, 166 28 Prague, Czech Republic

Abstract. Gold nanoparticles (Au NPs) were synthesized in single-crystalline yttria-stabilized zirconia (YSZ) using a high-energetic gold ion implantation with the intention of subsequent modification by silicon ion irradiation. (100)-oriented YSZ samples were implanted with 1 MeV Au⁺ ions at room temperature and fluences of $1.5 \times 10^{16} \text{ cm}^{-2}$, $5.0 \times 10^{16} \text{ cm}^{-2}$ and $7.5 \times 10^{16} \text{ cm}^{-2}$ and subsequently annealed for 1 h at 1100 °C in air. Gold NPs modification was realized with irradiation by 10 MeV Si³⁺ with the fluence of $5.0 \times 10^{14} \text{ cm}^{-2}$. Au NPs distribution and subsequent YSZ structure modification were studied. YSZ samples as-implanted with Au ions, annealed and subsequently irradiated with Si ions were characterized using Rutherford backscattering spectrometry (RBS) and RBS in channelling mode (RBS-C). The RBS spectra show that the implanted Au-ions concentrate in the YSZ sub-surface layer in the depth of about 50-250 nm and shift to greater depth with increasing ion fluence. The Si³⁺ ions irradiation slightly increased Zr sub-lattice disorder. Optical absorbance shows an increase of absorption band at 550 nm after Au implantation only for the two highest ion fluences. After annealing and Si irradiation, optical absorbance increased at 530-580 nm with connection to ion implantation fluence of Au⁺ ions.

1 Introduction

Gold nanoparticles (Au NPs) embedded in oxide matrices exhibit unique optical properties that can be used for a lot of applications, such as high-density information storage devices, ultrafast optical switches, and optical gas sensors [1]. The reliable production of such optical devices requires the ability to customize the optical response of the nanocomposite systems. In the case of gold (Au), the optical response of Au NPs is dominated by a surface plasmon resonance band (SPR), which exists due to the light-induced displacement of

* Corresponding author: miksova@ujf.cas.cz

conduction electrons to the positive ionic background in the NP [2]. The optical response of Au NPs is influenced by their shape, size, geometrical configuration, and composition [3]. The ion irradiation of the existing nanocomposite system can be used for the deformation of the NPs [4]. The threshold for Au NPs modification by subsequent energy transfer from energetic ions (electronic stopping power S_e), below which the Au nanoclusters remained spherical, depends on the particle size as well as on the substrate structure. For instance, modifications of Au NPs in silica with $d=15$ nm occur during irradiations by energetic ions with S_e of 3.5 keV/nm [5] and higher. For Au NPs in silica with 40–50 nm diameter, the electronic stopping power above 5.5 keV/nm is required for elongation. The elongation of Au NPs in silica with 80 nm diameter is observed for $S_e \sim 7\text{--}8$ keV/nm [6] (irradiated with high-energetic Ag and Cu ions). A similar value of 3.3 keV/nm was found in reference [5] for silica shell-Au core colloidal particles with identical sizes. In reference [7], a value of (2.0 ± 0.5) keV/nm was deduced for polydisperse Au particles in silica with $d < 14$ nm.

Ion implantation has an important role in the fabrication of nanoclusters embedded in materials. After heating to temperatures high enough that the implanted atoms become mobile, they will segregate from the matrix and form nanoclusters if the implantation depth is suitable compared to the migration distance [8]. Ytria-stabilized zirconia (YSZ) is widely used for advanced technological applications, such as thermal coating [9], gas sensors [10], or colourless ceramics in the jewellery [11] due to its distinctive features like high chemical stability and good radiation resistance. YSZ is also used as oxygen ion conductors, with applications in solid oxide fuel cells, oxygen pumps, and oxygen sensors. In these applications, YSZ functions as a solid electrolyte, where oxygen ions diffuse freely if the operating temperature is higher than required for the diffusion of oxygen ions ($T > 300$ °C) [12]. By adding Au NPs to YSZ, the diffusion kinetics of oxygen ions into the oxygen vacancies in the YSZ lattice is expected to increase as in general metals increase electrochemical reaction kinetics at the surfaces of doped YSZ electrodes [13].

This study focuses on the preparation of Au NPs created in YSZ by ion implantation using 1 MeV Au-ions and the subsequent irradiation is performed by 10 MeV Si^{3+} . It was shown that noble metals nanoparticles (Ag) can be effectively synthesized in YSZ by ion implantation [14]. Subsequent annealing was used for nanoparticle formation and the creation of Au: YSZ nanocomposite layers. Defect recovery in the nanocomposite layer will be discussed in connection to the annealing procedure and the additional energetic Si^{3+} ion irradiation. The structural and optical response of the prepared nanocomposite system in YSZ has been investigated using Rutherford backscattering spectrometry (RBS), RBS in channelling configuration (RBS-C), and optical measurement. While this methodology cannot replace the high-resolution analysis of implanted samples, it does offer a non-destructive, suitable, and cheaper alternative and complementary route for microscopy analysis when available.

2 Experimental set-up

The (100)-oriented YSZ fully stabilized with 9.5 mol. % Y_2O_3 (containing 1.5 wt. % Hf as the contaminant) were implanted with 1 MeV Au^+ ions at room temperature and fluences of $1.5 \times 10^{16} \text{ cm}^{-2}$, $5.0 \times 10^{16} \text{ cm}^{-2}$ and $7.5 \times 10^{16} \text{ cm}^{-2}$. An off-axis 7° regime to minimize the channelling effect and non-controllable Au dispersion into a deeper layer was used. An ion current density lower than $0.2 \mu\text{A} \cdot \text{cm}^{-2}$ was used to avoid target heating during implantation. Subsequent annealing in the air was performed for 1 h at 1100 °C. The irradiation by 10 MeV Si^{3+} (Si^+ listed below for simplicity) with the fluence of $5 \times 10^{14} \text{ cm}^{-2}$ was attempted to modify Au NPs shapes and distribution. All implantation experiments were carried out in the implantation chamber at the Tandetron Laboratory of the Nuclear

Physics Institute (NPI) in Řež (Czech Republic). A working pressure below 5.3×10^{-5} Pa was maintained by the pumping system based on a turbomolecular pump.

The Au concentration–depth profiles and structural modification were studied by Rutherford backscattering spectrometry (RBS) and RBS in channelling mode (RBS-C) using the beam of 2.8 MeV He^+ ions at the laboratory scattering angle of 170° with the depth probed of RBS $\sim 2 \mu\text{m}$ (in this geometry). Higher energy was used to differentiate Zr and Au signals in the RBS spectra. Random and aligned spectra (the spectrum of back-scattered ions with the ion beam incident along the crystallographic axis) were recorded using the defined rotation of the single-crystal sample which was mounted on the two-axis goniometer allowing for the rotation with a resolution of 0.01° . The ion currents used during the RBS analysis were ~ 5 nA. All samples were measured in three different spots to avoid additional damage during the measurements. The elemental concentration was analysed using the SIMNRA code [15].

The SRIM code [16] was used for the theoretical predictions of ion interaction with matter. Monte Carlo (MC) simulations performed with SRIM provided the calculated Au depth distribution in YSZ. The calculated results were compared to the experimental data. For a better understanding of electronic and nuclear stopping interplay in the implanted and subsequently irradiated YSZ, the SRIM simulations of energy losses were performed. Electronic and nuclear-energy stopping at various depths was calculated by simulating 1 MeV Au and 10 MeV Si penetrations through YSZ. The ratio between electronic and nuclear energy losses integrated into the whole penetration depth of ions was calculated as $S_e/S_n = 0.3$ (Au) and $S_e/S_n = 237$ (Si). In the surface region, the electronic stopping of Si ions predominate over nuclear ($S_e \sim 6.3$ keV/nm). Projected ranges and standard deviations of 1 MeV Au ions and 10 MeV Si were simulated by SRIM as follows: $R_p = 134$ nm and $\Delta R_p = 40$ nm, $R_p = 2.65 \mu\text{m}$ and $\Delta R_p = 225$ nm, respectively.

Optical absorption spectra were measured using Avantes AvaSpec-ULS-3648 Starline high-resolution fibre-optic spectrometer with linear CCD detector in the range of 250–600 nm at room temperature. As a source, a combined deuterium-halogen lamp Avalight-DHc was used. The light was guided from the source lamp using multimode optical fibre to the holder with the sample and the transmitted light was then collected with another multimode low-dispersion optical fibre into the detector. Optical absorption spectra were smoothed for better clarity and normalized to baseline in OriginPro 9.

3 Results and discussion

3.1 RBS-C method

The comparison of the aligned and the random RBS-C spectra of the pristine YSZ with as-implanted YSZ at the ion fluences of $1.5 \times 10^{16} \text{ cm}^{-2}$, $5.0 \times 10^{16} \text{ cm}^{-2}$ and $7.5 \times 10^{16} \text{ cm}^{-2}$ are shown in Figure 1a–c for the (100)-oriented YSZ sample, respectively. The random spectra exhibited in the high backscattering energy parts decrease in Zr signals. This decrease is connected to the presence of Au atoms confined in the thin region near the surface. This phenomenon is more pronounced after the Au-ion implantation at the highest fluence. In Figure 1, the decrease of Au signal in the aligned spectrum is connected to any Au preferential position in YSZ or shadowed with Zr atoms. A similar trend was observed in our previous work in ZnO [17]. Two disordered regions in the aligned RBS spectrum are shown: (i) the surface region connected to the modified YSZ surface region (~ 544 – 558 channels), and (ii) the deeper damage region (~ 490 – 530 channels) created after Au implantation (highlighted in the black rectangle). Figure 1 shows that the damaged region is

in a higher depth than is projected range of Au simulated by SRIM. It can be connected to defect migration during the ion implantation.

(i) In the surface damage region, a significant decrease of the Zr-disorder after the annealing for the two lower fluences was shown (Figures 1a and 1b – green line). After Si-ion irradiation disorder increases again (Figures 1a and 1b – blue line). In the case of $7.5 \times 10^{16} \text{ cm}^{-2}$, annealing did not contribute to the reconstruction of the surface damage region; on the contrary, an increase in damage was shown (see Figure 1c – green line). In subsequent Si^+ irradiated samples, the decrease of the disorder on the surface region was observed (see Figure 1c – blue line).

(ii) The damage accumulation in the deeper damage region was monitored using the normalised yields (χ_z) summarised in Figure 1d and Table 1 as a function of the Au-ion fluence. The values of χ_z are extracted from the RBS-C spectrum as the ratio of the yield in the aligned spectrum to the yield in the random spectrum in the highlighted region of interest (black rectangle) connected directly to Zr-sub-lattice disordering. The average value of χ_z for each sample was calculated from three measurements of χ_z as well as the statistical error of the mean $\Delta\chi_z$ [18].

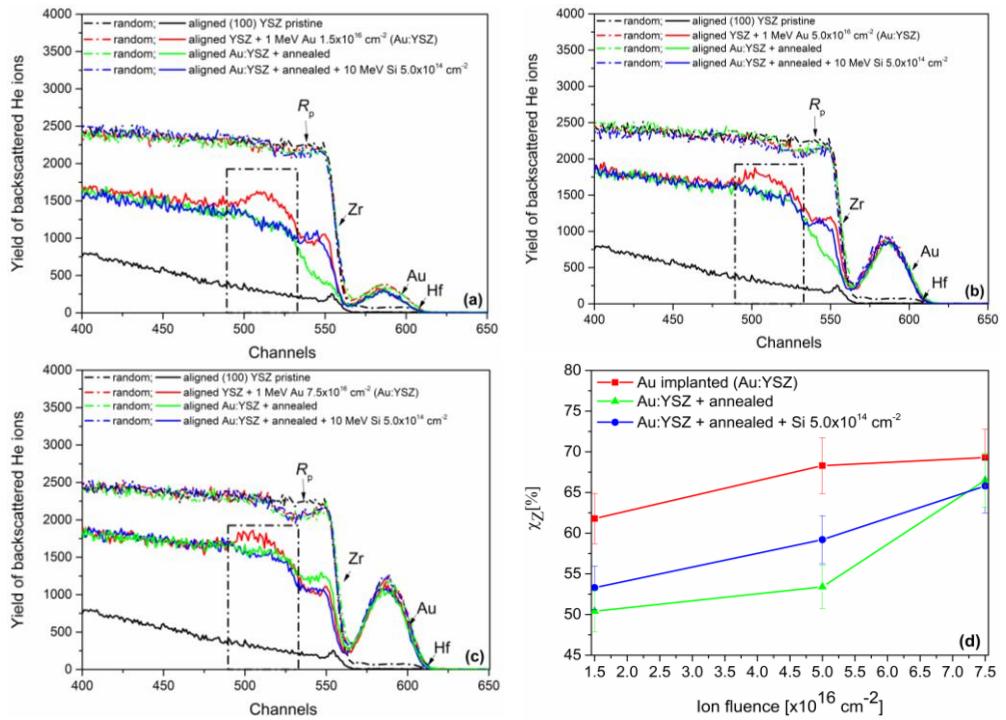


Fig. 1. The RBS-C spectra of the pristine, Au-implanted (with ion fluences of $1.5 \times 10^{16} \text{ cm}^{-2}$ (a), $5.0 \times 10^{16} \text{ cm}^{-2}$ (b) and $7.5 \times 10^{16} \text{ cm}^{-2}$ (c)), annealed and subsequently Si-irradiated YSZ at ion fluence of $5.0 \times 10^{14} \text{ cm}^{-2}$ for (100) orientation. The normalised yields (χ_z) are summarised as the function of Au^+ -ion fluence (d).

The increase of χ_z in the deeper damage region was observed with the increasing Au^+ ion fluence (Figure 1d – red line). After annealing, the crystalline structure of YSZ is partially healed (Figure 1d – green line); the Zr-disorder decrease is more pronounced for the lower

Au-ion implantation fluences, as was expected. Si-ion irradiation almost did not influence the value of χ_z in the deeper damage region (see Table 1).

The Au concentration-depth profiles were obtained in the Au-implanted, annealed and Si-irradiated samples from the RBS random spectra. The experimental Au concentration-depth profiles exhibit the normal distribution shape for all ion fluences, all projected ranges R_p and the standard deviation are shown in Table 1.

Tab. 1. The mean projected range R_p and the standard deviation ΔR_p deduce from the experimentally Au concentration-depth profiles from RBS. χ_z for YSZ implanted with Au-ions, annealed and subsequently irradiated with Si ions are presented in the last column.

(100) YSZ Fluence [Au ions.cm ⁻²]	Au implanted		annealed		Si irradiated	
	$R_p \pm \Delta R_p$ [nm]	$\chi_z \pm \Delta \chi_z$ [%]	$R_p \pm \Delta R_p$ [nm]	$\chi_z \pm \Delta \chi_z$ [%]	$R_p \pm \Delta R_p$ [nm]	$\chi_z \pm \Delta \chi_z$ [%]
1.5×10^{16}	151±45	61.8±3.1	156±46	50.4±2.5	157±46	53.3±2.7
5.0×10^{16}	161±63	68.3±3.5	169±62	53.4±2.7	168±62	59.2±3.0
7.5×10^{16}	184±73	69.3±3.6	181±72	66.5±3.4	180±70	65.8±3.2

The Au-concentration depth profiles are different from the calculated values with the projected range R_p calculated by SRIM-2013 as $R_p \pm \Delta R_p = 134 \pm 40$ nm. The experimental values of R_p and ΔR_p increase with the Au-ion implantation fluence. It was observed additional shifts of Au-maximum concentration to greater depth after the annealing, but after Si-ion irradiation, R_p is almost the same as after annealing (see Table 1). The maximum is shifted by about 30 % to the depth (~50 nm) for the Au implanted samples with the highest ion fluence. A similar trend was found in our previous work in Si implanted by Au⁺ ions [19], where the maximum shift is about 23 % (~35 nm). Discrepancies in the experimental Au-concentration depth profiles can be connected to overestimating electronic stopping in Au implemented in SRIM. It was mentioned in the study [20] that for heavy ions at low energy, the measurements of stopping show that SRIM electronic stopping is higher than the experimentally measured values. Nevertheless, there must be also taken into account the gradual modification of the YSZ structure during the implantation. Such a large shift, especially for the highest fluence, points to a certain Au migration.

3.2 Optical characterisation

Optical absorption spectra of the pristine YSZ samples (see Figure 2) showed the main absorption band around 280 nm (i.e. approx. 4.4 eV). From the literature, the optical band gap in YSZ, i.e. the energy transition between conduction and valence band, is 4.4–5.4 eV, i.e. 230–280 nm [21]. Optical absorption spectra of the samples Au-implanted YSZ are depicted in Figure 2a as well as results for samples, which were subsequently annealed at 1100 °C and Si-irradiated. The zoom of the region of interest in 450–680 nm wavelengths, where SPR peaks are localized, is presented in Figure 2b. The increase of the absorption band at around 550 nm was observed in Au implanted samples with fluence higher than 1.5×10^{16} cm⁻².

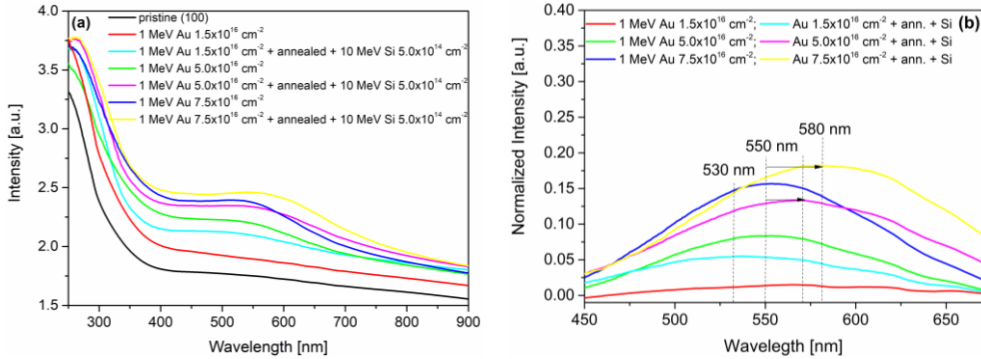


Fig. 2. Optical absorption spectra of the Au-implanted (100)-oriented YSZ (Au: YSZ) and Au: YSZ, annealed and Si-irradiated in the wavelength range from 250 to 900 nm and the zoom of the region of interest in 450–680 nm wavelengths is presented (b).

After annealing and Si-ion irradiation, the situation changed and the increase of the absorption band at the wavelength ~ 530 nm was observed for the lowest Au-ion fluence of $1.5 \times 10^{16} \text{ cm}^{-2}$ and at the wavelength between 570–580 nm for the two higher Au-ion fluences. This absorbance band can be attributed to gold nanoparticles (NPs) formation in YSZ [22,23], where the central wavelength can vary depending on the size of Au NPs. With increasing Au-ion implantation fluence, the absorption band centred at 550 nm increased as well. It can be connected to the enhanced nanoparticle creation (SPR activity) in the YSZ implanted and annealed layer, since the nanoparticle number increases with the increasing Au-ion fluence. However, we have to mention that the absorbance in the whole wavelength range increased as well, the YSZ samples became less transparent to visible light, which can be attributed to the creation of various extrinsic and intrinsic defects (vacancies, interstitials, etc.) in the structure of YSZ samples (defects caused the creation of new energy levels inside bandgap for optical absorption transitions). After the Si-ion irradiation, the absorbance band is shifted to the longer wavelengths about 580 nm and intensity increased. It can be ascribed to enhancing crystalline disorder as well as Au NPs clustering, or Au NPs size growth.

3.3 Discussion

(100)-oriented YSZ crystals were implanted with 1 MeV Au⁺ ions at ion fluences of $1.5 \times 10^{16} \text{ cm}^{-2}$, $5.0 \times 10^{16} \text{ cm}^{-2}$ and $7.5 \times 10^{16} \text{ cm}^{-2}$ and subsequently annealed at 1100 °C in the air for 1 hour. The Si-ion irradiation with energy 10 MeV was used to modify the created Au NPs. RBS, RBS-C and optical measurements on the produced samples were performed. It is shown from RBS, that the Au becomes distributed over a larger depth range with increasing Au ion fluence which can be connected to Au ion migration during ion implantation. The RBS-C showed higher damage in Zr-sublattice up to the projected range of Au ions in YSZ after the ion implantation. Subsequent annealing caused only partial healing of the crystalline YSZ structure, especially in the surface region (Figure 1a and 1b) and two lower ion fluences. 10 MeV Si-ion irradiation increased the disorder in the surface damage region, no additional disorder was observed in the deeper damage region. In the case of the highest Au ion fluence, the annealing caused the increase of disorder in the surface region and conversely reduced the damage in the surface region after Si-ion irradiation (Figure 1c).

The optical measurement showed the presence of Au NPs. Their growth was more pronounced for the two higher Au-ion fluences, where SPR peaks at 550 nm were shown.

No SPR peak was found for the lowest ion fluence. The band was previously connected with two defect types: oxygen vacancies with trapped electrons (F-type centres) nearest to Zr^{4+} cations and hole trapped oxygen ions (V-type centres) adjacent to Y^{3+} cations [24]. After annealing and Si-ion irradiation, the shift of SPR to higher wavelengths (~ 580 nm) was observed (Figure 2b) for the two higher ion fluences. It was connected to Au NPs clustering or increasing the size of NPs [25]. For the lowest ion fluence, the SPR peak was observed at ~ 530 nm (Figure 2b – turquoise line), which correspond to Au NPs formation after annealing. Further analysis is needed to reach satisfactory conclusions about the size and distributions of Au NPs.

4 Conclusions

The YSZ samples were implanted with 1-MeV Au^+ ions over a broad ion-implantation fluence range at RT. These samples were characterised by RBS, RBS-C, and optical measurement. The combination of these analytical methods provides advantages for a better understanding of structural modifications upon implantation and subsequent annealing and Si^{3+} ions irradiation. The study shows that the formation of Au NPs occurs before annealing especially for ion fluence from $5.0 \times 10^{16} \text{ cm}^{-2}$ and that annealing and Si irradiation cause the formation of Au NPs even for the lowest Au fluence ($1.5 \times 10^{16} \text{ cm}^{-2}$).

The research has been carried out at the CANAM (Centre of Accelerators and Nuclear Analytical Methods) infrastructure LM 2015056. This publication has been supported by OP RDE, MEYS, Czech Republic, under the project CANAM OP, CZ.02.1.01/0.0/0.0/16_013/0001812.

References

1. G. Sirinakis, R. Siddique, K.A. Dunn, H. Efstathiadis, M.A. Carpenter, A.E. Kaloyeros, L. Sun, *J. Mater. Res.* 20, 3320–3328 (2005)
2. U. Kreibig, M. Vollmer, *Optical Properties of Metal Clusters*, Springer Berlin Heidelberg, Berlin, Heidelberg, 1995.
3. L. Montaña-Priede, O. Peña-Rodríguez, A. Rivera, A. Guerrero-Martínez, U. Pal, *Nanoscale*. 8, 14836–14845 (2016)
4. A.A. Leino, F. Djurabekova, K. Nordlund, *Eur. Phys. J. B.* 87, 242 (2014)
5. J.J. Penninkhof, T. van Dillen, S. Roorda, C. Graf, A. van Blaaderen, A.M. Vredenberg, A. Polman, *Nuclear Instruments and Methods in Physics Research Section B: Beam Interactions with Materials and Atoms.* 242, 523–529 (2006)
6. E.A. Dawi, A.M. Vredenberg, G. Rizza, M. Toulemonde, *Nanotechnology*. 22, 215607 (2011)
7. C.H. Kerboua, J.-M. Lamarre, M. Chicoine, L. Martinu, S. Roorda, *Thin Solid Films.* 527, 186–192 (2013)
8. F. Ren, X.H. Xiao, G.X. Cai, J.B. Wang, C.Z. Jiang, *Appl. Phys. A.* 96, 317–325 (2009)
9. P. Wright, *Current Opinion in Solid State and Materials Science.* 4, 255–265 (1999)
10. S. Park, J.M. Vohs, R.J. Gorte, *Nature.* 404, 265–267 (2000)
11. Y. Saito, Y. Imamura, A. Kitahara, *Nuclear Instruments and Methods in Physics Research Section B: Beam Interactions with Materials and Atoms.* 206, 272–276 (2003)
12. N. Docquier, S. Candel, *Combustion control and sensors: a review*, *Progress in Energy and Combustion Science.* 28, 107–150 (2002)
13. P.H. Rogers, G. Sirinakis, M.A. Carpenter, *J. Phys. Chem. C.* 112, 8784–8790 (2008)

14. R. Mikšová, A. Jagerová, P. Malinský, P. Harcuba, J. Veselý, V. Holý, U. Kentsch, A. Macková, *Vacuum*. 184, 109773 (2021)
15. M. Mayer, SIMNRA, a simulation program for the analysis of NRA, RBS and ERDA, in: *AIP Conference Proceedings*, AIP, Denton, Texas (USA), 1999: pp. 541–544.
16. J.F. Ziegler, M.D. Ziegler, J.P. Biersack, SRIM – The stopping and range of ions in matter, *Nuclear Instruments and Methods in Physics Research Section B: Beam Interactions with Materials and Atoms*. 268, 1818–1823 (2010)
17. A. Macková, P. Malinský, A. Jagerová, R. Mikšová, P. Nekvindová, J. Cajzl, R. Böttger, S. Akhmadaliev, *Vacuum*. 169, 108892 (2019)
18. G. Bohm, G. Zech, *Introduction to statistics and data analysis for physicists*, Verl. Dt. Elektronen-Synchrotron, Hamburg, 2010.
19. R. Mikšová, A. Macková, A. Jagerová, P. Malinský, P. Slepíčka, V. Švorčík, *Applied Surface Science*. 458, 722–733 (2018)
20. H. Paul, Nuclear stopping power and its impact on the determination of electronic stopping power, in: Ft. Worth, TX, USA, 2013: pp. 309–313.
21. X. Hong, S. Xu, X. Wang, D. Wang, S. Li, B.A. Goodman, W. Deng, *Journal of Luminescence*. 231, 117766 (2021)
22. X. Huang, M.A. El-Sayed, *Journal of Advanced Research*. 1, 13–28 (2010)
23. V. Morandi, F. Marabelli, V. Amendola, M. Meneghetti, D. Comoretto, *Adv. Funct. Mater.* 17, 2779–2786 (2007)
24. S. Zhu, X.T. Zu, X. Xiang, Z.G. Wang, L.M. Wang, R.C. Ewing, *Nuclear Instruments and Methods in Physics Research Section B: Beam Interactions with Materials and Atoms*. 206, 1092–1096 (2003)
25. S. Link, M.A. El-Sayed, *J. Phys. Chem. B*. 103, 4212–4217 (1999)